Applied Catalysis A, General 708 (2025) 120582

Contents lists available at ScienceDirect

Applied Catalysis A, General

journal homepage: www.elsevier.com/locate/apcata

Revealing the characteristics of supported Ni-Mn based mixed metal oxide catalysts: *Operando* insights into their activation and CO_2 methanation behavior

Dennis Weber [a,d], Timo Engl [b], Malte Raabe [a], Andreas Hutzler [c], Michael Rubin [b], Roland Dittmeyer [b], Tanja Franken [a,d,*]

[a] *Department of Chemical and Biological Engineering, Institute of Chemical Reaction Engineering, Assistant Professorship for Catalytic and Electrocatalytic Systems and Processes, Friedrich-Alexander-Universität, Erlangen-Nürnberg, Egerlandstraße 3, Erlangen 91058, Germany*

[b] *Institute for Micro Process Engineering (IMVT), Karlsruhe Institute of Technology (KIT), Hermann-von-Helmholtz-Platz 1, Eggenstein-Leopoldshafen 76344, Germany*

[c] *Forschungszentrum Jülich, Helmholtz-Institute Erlangen-Nürnberg for Renewable Energy, Cauerstraße 1, Erlangen 91058, Germany*

[d] *Technische Universität Darmstadt, Ernst-Berl-Institut für Technische und Makromolekulare Chemie, Technische Chemie 1, Peter-Grünberg-Straße 8, Darmstadt 64287, Germany*

ARTICLE INFO

Keywords:
CO_2 Methanation
Mixed metal oxides
Catalysis
Operando

ABSTRACT

Power-to-gas technologies, such as CO_2 methanation, enable to mitigate man-made climate change. For this process to be viable, it is essential to use an active, selective and stable catalyst. This study addresses these requirements by creating a novel Ni-Mn_yO_x/Al_2O_3 ($0 \leq y \leq 1$) catalyst that uses Mn not as a dopant but creates a joined Ni-Mn mixed metal oxide (MMO) phase on a Al_2O_3 support. To identify the ideal composition, we compare different Mn contents y from 0 to 1 and determine an Mn/Ni ratio of 0.375 as the minimum for the formation of the supported Ni-Mn MMO phase. Compared to the self-synthesized, literature-based state-of-the-art type NiO_x/Al_2O_3 based CO_2 methanation catalysts the Ni-Mn MMO based catalysts achieve about 30 % higher Ni specific methane formation rates. We carefully characterize the catalysts phase composition, surface area, active metal surface area, reducibility, surface basicity and elemental analysis. Additionally, we present a detailed *in situ* X-ray absorption spectroscopy (XAS) study and phase characterization on the reduction process for catalytic activation of the calcined catalysts to draw conclusions on the final activated state. It was shown that the Ni-Mn mixed metal oxide phase changes upon activation into metallic Ni supported on a Ni-depleted Ni-Mn MMO phase. Additionally, the behavior of both catalysts under reaction conditions was investigated using *operando* XAS, phase analysis and Diffuse Reflectance Infrared Fourier Transform Spectroscopy. Based on this, a tentative reaction mechanism was proposed which includes the possibility of additional CO_2 activation pathways on the Ni-Mn MMO phase.

1. Introduction

A major challenge for today's society is the mitigation of anthropogenic climate change caused by the continued burning of fossil fuels and the resulting emissions of greenhouse gases, especially CO_2 [1,2]. One promising technology contributing to the transition to a future energy system with low carbon dioxide footprint is Power-to-Gas, which includes CO_2 methanation (1), also known as the Sabatier reaction [3]. This process produces methane using renewable hydrogen, which can be integrated into existing infrastructure for subsequent utilization [4–6].

$$CO_2 + 4H_2 \rightleftharpoons CH_4 + 2H_2O,\ \Delta_R H = -165.0 kJmol^{-1} \quad (1)$$

The CO_2 required for methanation may come from industrial waste gases with high concentrations, such as those emitted from cement production or waste incineration plants [7]. However, to achieve net zero emissions and create a circular carbon economy, technologies to remove CO_2 from the atmosphere will be essential in the future. These technologies can provide a source of CO_2 for both storage (carbon capture and storage, CCS) and utilization (carbon capture and utilization, CCU) as a feedstock for various processes [5,8,9]. In a scenario

* Corresponding author at: Department of Chemical and Biological Engineering, Institute of Chemical Reaction Engineering, Assistant Professorship for Catalytic and Electrocatalytic Systems and Processes, Friedrich-Alexander-Universität, Erlangen-Nürnberg, Egerlandstraße 3, Erlangen 91058, Germany.
E-mail address: tanja.franken@tu-darmstadt.de (T. Franken).

https://doi.org/10.1016/j.apcata.2025.120582
Received 16 May 2025; Received in revised form 16 September 2025; Accepted 17 September 2025
Available online 20 September 2025

where green hydrogen and CO_2 from non-fossil sources are utilized, the conversion processes will require flexibility in terms of load and rather unconventional scales of implementation, such as smaller decentralized plants rather than conventional large-scale chemical plants. To tailor the accordant processes, it is of crucial importance to find suitable catalysts with high reactivity and to understand the reaction mechanism and kinetics.

Ni/Al_2O_3 is the state-of-the art catalyst for CO_2 methanation due to its high selectivity and cost efficiency. Ni-sintering and the probable formation of the more stable $NiAl_2O_4$ spinel phase on the surface lead to a decrease in catalytic activity and selectivity [10–13]. To improve the stability and productivity of this catalyst system, many different promoters have been tested. Especially Mn and Fe were studied as promoters for supported catalysts [14–19]. In addition, these elements were also used in larger quantities in bulk catalysts, resulting in various mixed metal oxides (MMO) [12,20–22].

For supported catalysts Mn was only added in small quantities ($\leq$ 5 wt%) as a promoter. It has been reported that at these small amounts, Mn is present as a separate MnO_x phase adjacent to the Ni phase and acts as a spacer, resulting in an improved Ni dispersion and thus increasing catalytic performance, with a further slight increase in performance observed with increasing Mn content [14–16,18,19]. To the best of our knowledge, the effects of higher manganese contents (> 5 wt%) on the structural properties and catalytic behavior of simultaneously supported Mn and Ni on Al_2O_3 are not yet known, especially regarding the Ni-Mn interaction, activation and the resulting catalytic performance. This study is intended to provide exactly these missing insights.

The reaction mechanism of CO_2 methanation remains a topic of debate in the literature, with variations depending on the catalyst type, support material, and promoter. CO_2 adsorption and activation can occur either on the support or on the catalytically active metal, leading to the formation of different intermediates, such as carbonate, bicarbonate (hydrogen carbonate), carbonyl or formate species [16,23–25]. Depending on the catalyst, reaction mechanisms are proposed that are either analogous to the CO methanation or take place via a formate-mediated route. For reducible supports, such as CeO_2, ZrO_2 and MnO_x, the possibility to induce defects/oxygen vacancies enables an alternative reaction route involving carbonate and formate intermediates [26–29].

In this study, we go beyond previous work by introducing higher Mn contents (up to 14 wt%) resulting in a novel $Ni\text{-}Mn_yO_x/Al_2O_3$ catalyst. To identify the optimal composition, the Mn content y was varied in the range from 0 to 1. With the help of *operando* XAS and XRD the phase changes upon activation as well as the changes of the catalysts during methanation were investigated and with the help of *operando* DRIFTS data, the differences in the reaction mechanism between a $Ni\text{-}Mn_yO_x/Al_2O_3$ catalyst and a literature-based state-of-the-art type NiO_x/Al_2O_3 are discussed.

2. Results and discussion

2.1. Characterization of $Ni\text{-}Mn_yO_x/Al_2O_3$ catalyst

All catalysts were prepared by incipient wetness impregnation. For the $Ni\text{-}Mn_yO_x/Al_2O_3$ catalysts, the amount of Ni nitrate was adjusted to achieve the desired loading of 15 wt% Ni and the amount of Mn nitrate corresponding to the desired Mn/Ni ratio. Inductively coupled plasma atomic emission spectroscopy (ICP-AES) confirms the desired loadings and Mn/Ni ratios (see Table 1). For the manganese-free sample, X-ray diffraction (XRD) shows the presence of NiO (ICSD: 98–008–7108) and γ-Al_2O_3 phases (ICSD: 98–009–9836), as expected (Fig. 1). Accordingly, no significant crystalline spinel phase $NiAl_2O_4$ was formed, as the Al_2O_3 reflections showed no shift, and no high-temperature peak was observed in the temperature programmed reduction (TPR) (Fig. 2). The XRD pattern (Fig. 1) for the $Ni\text{-}Mn_{0.125}O_x/Al_2O_3$ catalyst also shows only NiO and γ-Al_2O_3 phases and no crystalline Mn phase, which is most likely due to the low manganese content. This has also been shown by Vrijburg and others for similar systems with low manganese content ($\leq$ 5 wt% Mn) [16,18,19].

As the manganese content increases, the NiO phase visually disappears and a hexagonal $MnNiO_3$-like mixed metal oxide (ICSD: 98–003–1853) phase forms starting from a Mn/Ni ratio of 0.375 (> 5 wt % Mn, see Fig. 1), which can be identified by the non-overlapping reflections at $2°\Theta = 24.7°$, 33.8°, 50.6° and 55.2°, as well as by the oxidation states of Ni and Mn in the X-ray absorption (XAS) (see Figure S1 & S2). In the Fourier transformed extended X-ray absorption fine structure (FT-EXAFS) spectra for the NiO_x/Al_2O_3 and $Ni\text{-}Mn_1O_x/Al_2O_3$ the contributions of Ni-O (1.5–1.6 Å) and $Ni\text{-}Ni_{ox}$ (2.5 Å) are visible, as in the NiO pellet (Figure S3), although the Ni-O distance for the Ni-Mn MMO-containing catalyst is slightly shifted compared to the NiO pellet, which also shows the phase differences. Therefore, all catalysts with an Mn/Ni ratio of 0.375 and more are referred to as Ni-Mn

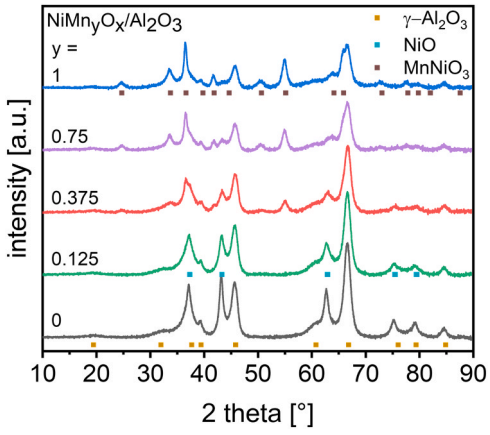

Fig. 1. XRD patterns of $Ni\text{-}Mn_yO_x/Al_2O_3$ catalyst with increasing Mn content y.

Table 1
Specific surface area and pore volume measured by N_2 physisorption, elemental composition measured by ICP-AES and $MnNiO_3$/NiO phase ratio estimated from XRD by the semi-quantitative reference intensity ratio method of the different catalysts [30].

Sample	Specific surface area S_{BET} [$m^2\ g^{-1}$]	Porevolume[$cm^3\ g^{-1}$]	Elemental analysis			$MnNiO_3$/NiO phase ratio [-]
			Ni [wt%]	Mn [wt%]	Mn/Ni ratio	
Al_2O_3	141	1.02	0.0	0.0	-	-
MnO_x/Al_2O_3	99	0.72	0.0	13.7	-	-
NiO_x/Al_2O_3	100	0.71	14.4	0.0	-	-
$Ni\text{-}Mn_{0.125}O_x/Al_2O_3$	100	0.70	15.2	1.8	0.118	0.08
$Ni\text{-}Mn_{0.375}O_x/Al_2O_3$	104	0.64	14.8	5.7	0.385	0.30
$Ni\text{-}Mn_{0.75}O_x/Al_2O_3$	100	0.54	14	10.5	0.750	5.25
$Ni\text{-}Mn_1O_x/Al_2O_3$	96	0.54	13.8	13.8	1.000	10.11

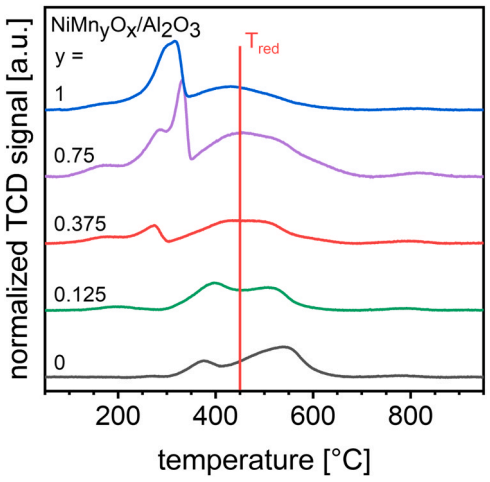

Fig. 2. TPR profiles of Ni-Mn_yO_x/Al_2O_3 catalyst with increasing Mn content y. Conditions: 10 % H_2 in Ar with a flow rate of 50 ml min^{-1}, Ramp: 5 K/min.

MMO containing catalysts.

As the Mn content increases, the phase ratio of $MnNiO_3$/NiO increases quickly (see Table 1), so that at a Mn/Ni ratio of 1, the crystalline NiO phase visually disappeared in the XRD pattern (Fig. 1) and the $MnNiO_3$ phase remained the solely phase supported on Al_2O_3. The specific surface area S_{BET} remains constant for all Mn/Ni ratios, although the metal content on the support doubles when comparing NiO_x/Al_2O_3 and Ni-Mn_1O_x/Al_2O_3 (see Table 1). Meanwhile, the pore volume decreases with higher metal loadings, which seems to indicate that the resulting $MnNiO_3$ phase has a higher specific surface area than the NiO phase and thus compensates for the decrease in the accessible specific surface area of the support. In contrast to S_{BET}, the Mn/Ni ratio had a major influence on the active Ni surface area A_{Ni}, which was estimated by N_2O titration. To exclude a contribution of Mn to the measurement of the Ni surface area, MnO_x/Al_2O_3 was also tested in the N_2O titration and showed no N_2 signal (see Eq. (3)).

If reduced NiO_x/Al_2O_3 and Ni-$Mn_{0.125}O_x/Al_2O_3$ are compared, the modification with manganese leads to an almost fourfold increase of A_{Ni}, whereby A_{Ni} decreases with Mn/Ni ratios above 0.125 but stays at a high level compared to NiO_x/Al_2O_3 (Table 2). The decrease of the active Ni surface area with increasing Mn/Ni ratio can be attributed to the formation of the $MnNiO_3$ phase (see Fig. 1), which remained as a modified MMO even after the reduction of the catalyst and during methanation (see Figure S4) and hence maintains a part of Ni in the oxidized state. In contrast to the decreasing A_{Ni}, the CO_2 adsorption capacity, measured by temperature programmed desorption of CO_2 (CO_2-TPD), increases with increasing Mn/Ni ratio by up to 30 % in comparison with the NiO_x/Al_2O_3 supported catalyst. In addition, as the Mn/Ni ratio increased, more weak (100–200 °C) basic sites were formed, while the number of medium (200–400 °C) and strong (> 400 °C) basic sites did not change significantly (Table 3, Fig. 3 and Figure S5-6).

Table 2
H_2 uptake measured by TPR and active Ni surface area after pretreatment according to catalytic tests measured by N_2O titration of the different catalysts.

Sample	H_2 uptake upon reduction [mmol g_{cat}^{-1}]	Normalized active Ni surface area $A_{Ni,norm}$ [m^2 g_{cat}^{-1}]
Al_2O_3	-	0.0
MnO_x/Al_2O_3	2.1	0.0
NiO_x/Al_2O_3	0.7	1.6
Ni-$Mn_{0.125}O_x/Al_2O_3$	1.4	5.7
Ni-$Mn_{0.375}O_x/Al_2O_3$	2.1	5.5
Ni-$Mn_{0.75}O_x/Al_2O_3$	3.0	4.8
Ni-Mn_1O_x/Al_2O_3	3.6	4.1

2.2. Catalytic behavior of NiO_x/Al_2O_3 and Ni-Mn_yO_x/Al_2O_3 catalysts

For the experiments conducted in the fixed bed reactor, a high space velocity (SV) of 26.2 ml min^{-1} mg_{cat}^{-1} was chosen to increase the stress on the catalyst for evaluation of reaction rates, to stay far away from the thermodynamic equilibrium and to analyse the stability, i.e. test for potential deactivation. All the catalysts tested showed almost no deactivation in the 40-hour stability tests (Figure S7). Long-term tests in the DRIFTS reactor were performed, showing that the modified catalyst stays quite stable, while the NiO_x/Al_2O_3 catalyst did undergo some deactivation (Figure S8). MnO_x/Al_2O_3 has no activity in CO_2 methanation (results not shown), confirming that Mn alone is not an active site.

The modification with manganese leads to an tremendous increase in catalytic performance, namely at least a tripling of the methane formation rate compared to the NiO_x/Al_2O_3 catalyst (Table 4 and Fig. 4). All Ni-Mn MMO containing catalysts exhibit higher methane formation rates at 350 °C, also per g_{Ni} in the catalyst, than comparable supported catalyst systems reported in the literature (Table 5 and Table S1). The CO_2 conversion and CH_4 selectivity are not easily comparable between different publications as they strongly depend on the catalyst pretreatment and the reaction conditions used (e.g. SV, catalyst mass etc.) (see Table 5 and Table S1). Further comparisons can be found in the supporting information by Rui et al. [31].

The increase in methane yield for the catalyst with low Mn content (Ni-$Mn_{0.125}O_x/Al_2O_3$), is mainly due to the larger Ni surface, with the separate MnO_x phase presumably acting as a spacer, as observed in other publications [14–16,18,19]. This is evident, as the Ni-$Mn_{0.125}O_x/Al_2O_3$ catalyst has the largest Ni surface area of all catalysts tested, but not the highest methane formation rate. It also exhibits a comparable methane formation rate and yield related to the available Ni metal surface area derived from N_2O-titration (Ni specific methane formation rate) to that of the NiO_x/Al_2O_3 reference catalyst (Tables 2 and 4). Moreover, the high Ni surface area of the Ni-$Mn_{0.125}O_x/Al_2O_3$ catalyst could lead to increased dissociative CO_2 adsorption on Ni^0. According to Schmider et al. [32], the dissociative adsorption of CO_2 on a Ni based catalyst has an activation energy of 89.3 kJ mol^{-1}, which is comparable to the apparent activation energy determined in the present study for Ni-$Mn_{0.125}O_x/Al_2O_3$.

All Ni-Mn MMO containing supported catalyst exhibited similarly high Ni specific methane formation rates and yields and outperformed the non Ni-Mn MMO containing catalysts (NiO_x/Al_2O_3 and Ni-$Mn_{0.125}O_x/Al_2O_3$) by about 31 % (see Table 4). The improved catalytic performance of the Ni-Mn MMO catalysts can therefore not be solely explained by the differences in Ni surface area. This suggests that the Ni-

Table 3
Adsorbed amount of CO_2 measured by CO_2-TPD for the different reduced catalysts.

Sample	Weak basic sites [mmol g^{-1}]	Medium basic sites [mmol g^{-1}]	Strong basic sites [mmol g^{-1}]	Total basic sites [mmol g^{-1}]
Al_2O_3	0.13	0.29	0.35	0.77
MnO_x/Al_2O_3	0.17	0.22	0.34	0.73
NiO_x/Al_2O_3	0.12	0.27	0.31	0.70
Ni-$Mn_{0.125}O_x/Al_2O_3$	0.17	0.24	0.35	0.76
Ni-$Mn_{0.375}O_x/Al_2O_3$	0.21	0.25	0.39	0.85
Ni-$Mn_{0.75}O_x/Al_2O_3$	0.24	0.22	0.40	0.86
Ni-Mn_1O_x/Al_2O_3	0.28	0.22	0.37	0.87

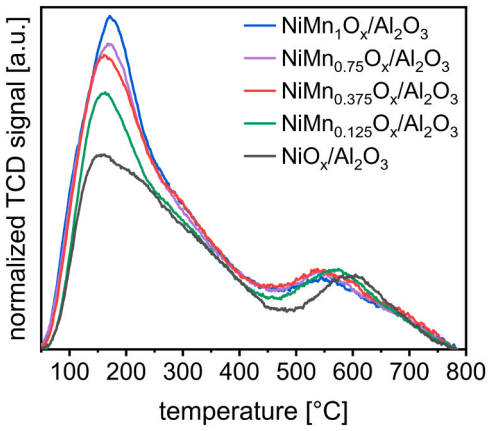

Fig. 3. CO_2-TPD profiles of Ni-Mn_yO_x/Al_2O_3 catalysts with increasing Mn content y. Conditions: Ramp: 5 K min^{-1} in He, pretreatment: 10 % H_2 in Ar with a flow rate of 50 ml min^{-1} at 450 °C for 1 h, adsorption: pure CO_2 with a flow rate of 20 ml min^{-1} at 100 °C for 1 h.

Table 4
Methane formation rates at 375 °C and apparent activation energies for the different reduced catalysts.

Sample	Methane formation rate r_{CH_4} at 375 °C [mol(CH_4) h^{-1} g_{cat}^{-1}]	Ni specific methane formation rate at 375 °C [mol(CH_4) h^{-1} m_{Ni}^{-2}]	Apparent activation energy [kJ mol^{-1}]
NiO_x/Al_2O_3	0.26	0.16	79 ± 2
Ni-$Mn_{0.125}O_x$/Al_2O_3	0.91	0.16	91 ± 2
Ni-$Mn_{0.375}O_x$/Al_2O_3	1.15	0.21	83 ± 2
Ni-$Mn_{0.75}O_x$/Al_2O_3	1.03	0.21	80 ± 2
Ni-Mn_1O_x/Al_2O_3	0.84	0.20	76 ± 2

Mn MMO phase contributes to their activity. Furthermore, there is a significant influence of the Ni-Mn MMO phase on the apparent activation energy of the different catalysts, as the apparent activation energy decreases with increasing Ni-Mn MMO phase content (see Table 4), which could indicate changes in the reaction mechanism. However, the Ni-specific methane formation rates and apparent activation energies are very similar for the various Ni-Mn containing MMO catalysts (Table 4), which indicates that for these catalysts the differences in catalytic performance are due to the differences in the number of active Ni sites. Therefore, the further *operando* investigations were only carried out with the non MMO containing NiO_x/Al_2O_3 reference catalyst as well as one of the MMO containing catalysts (Ni-Mn_1O_x/Al_2O_3). The Ni-Mn_1O_x/Al_2O_3 catalysts was chosen, because it contains the largest amount of the $MnNiO_3$ MMO phase and has only minor side phases complicating the interpretation.

Additionally, basicity is often considered a key property for a highly active catalyst system for CO_2 methanation, with weak and medium basic sites being identified as crucial[12,16,25,33]. As the Mn/Ni ratio increases more weak basic MnO_x sites are available in the methanation temperature range, resulting in an increased CO_2 adsorption capacity (Table 2), while simultaneously the Ni surface area decreases. This increase in CO_2 adsorption capacity and the possible changes in the CO_2 activation could partially offset the performance loss due to reduction of the active Ni surface area associated with increasing Ni-Mn MMO content, resulting in comparable performance across all Mn containing catalysts.

The comparison of Ni-Mn_1O_x/Al_2O_3 and NiO_x/Al_2O_3 in the diffuse reflectance infrared Fourier transform spectroscopy (DRIFTS) reactor also confirms these results at elevated pressure (5 bar(a)), with the methane yield of the Ni-Mn MMO catalyst also exceeding the non-modified NiO_x/Al_2O_3 catalyst by a factor of almost 3 at 375 °C (see Figure S9). These results and their implications, together with the results of the *operando* DRIFTS experiments, are further discussed in the reaction mechanisms section.

2.3. Activation of NiO_x/Al_2O_3 and Ni-Mn_yO_x/Al_2O_3 catalyst

The activation behavior of the Ni-Mn_yO_x/Al_2O_3 catalysts was investigated utilizing various TPR experiments, including combined *in-situ* TPR-XAS/XRD experiments, as this has a crucial impact on their catalytic performance. TPR shows that NiO_x/Al_2O_3 exhibits two reduction peaks, a low-temperature peak for large, weakly bound NiO particles and a high-temperature peak corresponding to either small, more strongly bound NiO particles or a spinel-like surface structure (Fig. 2) [36]. For the Ni-$Mn_{0.125}O_x/Al_2O_3$ catalyst, a small low-temperature peak is observed in the TPR, and in comparison with the NiO_x/Al_2O_3 catalyst the total amount of hydrogen used in the reduction is increased (Fig. 2 and Table 2). Among others, Vrijburg et al. showed for a similar system that the introduction of Mn (Mn/Ni: 0.25) can facilitate the reduction of Ni and improve Ni dispersion compared to the NiO_x/Al_2O_3 catalyst[14,16,18,19].

For the Ni-Mn MMO containing catalysts, an additional second and third low-temperature peak was observed, both of which were more pronounced with increasing Mn content (see Fig. 2). These peaks could be mainly attributed to the phase transformation into the Ni-depleted $Mn_{0.75}Ni_{0.25}O$ (ICSD: 98–006–1322) structure using *in situ* TPR-XRD (see Fig. 5 and Figure S4). This is also confirmed by comparing the Mn-K edge before and after reduction with MnO and MnO_2, as the Mn-K edge shows a complete reduction of Mn^{4+} to Mn^{2+} during the phase transition, as does the linear combination fit (LCF) of the Mn and Ni K-edge of the *in situ* TPR-XAS and FT-EXAFS results (Fig. 6 and Figure S1 and S10-11). In the *in situ* TPR-XRD of Ni-Mn_1O_x/Al_2O_3, Ni is barely visible (Fig. 5 A), which is probably due to the relatively fast heating ramp of 10 K min^{-1}. This is confirmed by *operando* CO_2 methanation XAS (LCF) and XRD experiments, where Ni is clearly visible ($2\Theta = 7.2°$) after reduction and becomes even more pronounced during methanation (see Figure S4 and S13). To further confirm this, the reduction of NiO_x/Al_2O_3 and Ni-Mn_1O_x/Al_2O_3 was repeated *ex situ* at 450 °C with 1 h holding time according to the pretreatment conditions. As expected, Ni (ICSD: 98–007–6667) reflections could be detected at $2\Theta = 44.4°$, 51.7°, 76.1° for both catalysts (see Fig. 5 B) and Figure S12 In summary, the above mentioned characterization methods show that upon activation of the Ni-Mn_1O_x/Al_2O_3 catalyst, some Ni is available as metallic Ni, but a significant amount of Ni remains in the $Mn_{0.75}Ni_{0.25}O$ MMO phase.

The partial reduction of Ni can also be seen from the *in situ* TPR-XAS experiments, as the pre-edge of both catalysts shifts towards lower energies and the normalized intensity of the edge is reduced (Figure S10), which is consistent with the difference between Ni foil and NiO (Figure S2). This is also evident from the FT-EXAFS spectra, because even after activation a significant contribution of Ni-O (1.5–1.6 Å) and Ni-Ni_{ox} (2.5 Å), as in the oxidized catalysts and the NiO pellet, is still visible.

For the NiO_x/Al_2O_3 catalyst, most of the NiO was reduced to Ni under the pretreatment conditions. This can be seen from the LCF of the Ni K-edge of the *in situ* TPR-XAS (Fig. 7) and the LCF of the *operando* methanation experiments (Figure S13A) as well as from the XRD of the *ex situ* reduced sample (see Figure S12). Similar trends were observed in the FT-EXAFS spectra. For the reduced NiO_x/Al_2O_3 catalysts, the Ni-Ni_{red} (2.1 Å) features as in the Ni foil (compare Figs. 6–7 and Figure S3) seems to be more pronounced than that of the Ni-Mn_1O_x/Al_2O_3 catalysts, which is in line with the *in situ* TPR-XAS and XRD results. In addition, for both catalysts, a slight change in the spectra towards more reduced Ni after CO_2 methanation compared to the spectra after the initial reduction can also be seen in the FT-EXAFS data (see Fig. 6B and

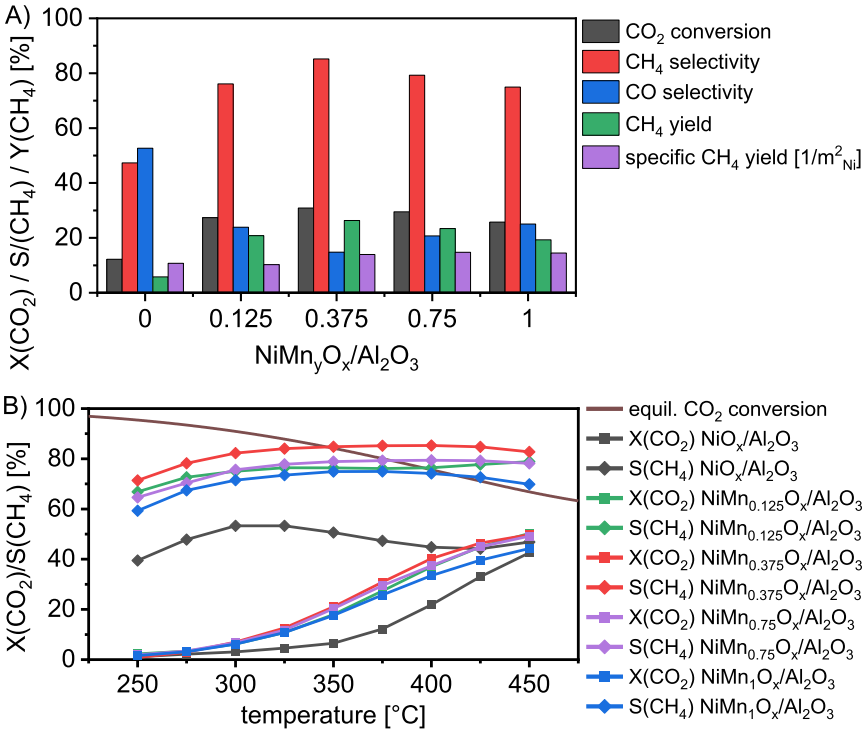

Fig. 4. A) & B) Catalytic performance comparison of Ni-Mn_yO_x/Al_2O_3 catalysts in methanation of CO_2 (A: T = 375 °C). Conditions: Pretreatment: 10 % H_2 in Ar at 450 °C for 1 h, methanation: c(CO_2) = 6.25 vol%, CO_2/H_2 = 1/4 diluted in Ar, m(cat) = 20 mg diluted in 2.5 g quartz sand, total flow rate: 523.6 ml min^{-1}, GHSV = 20000 h^{-1}, SV = 26.18 ml min^{-1} mg_{cat}^{-1},p = 1 bar.

Fig. 7B).

The scanning transmission electron microscopy (STEM) images (Fig. 8 and Figure S14-15) of the calcined and reduced NiO_x/Al_2O_3 catalyst show a broad size range of NiO particle sizes, leading after activation to a similarly broad distribution of Ni nanoparticles with significantly larger particles. The STEM images of the reduced Ni-Mn_1O_x/Al_2O_3 catalyst show that much smaller Ni particles with higher dispersion are obtained after the reduction of the Ni-Mn MMO containing catalyst (Table 1, Fig. 9 and Figure S16). The Ni nanoparticles probably dissolve from the Ni-Mn MMO phase upon activation, and because they are atomically dispersed there (see Figure S17), much smaller Ni nanoparticles can form upon reduction, resulting in a larger active Ni surface area, as demonstrated by the N_2O titration results.

2.4. *Operando DRIFTS of NiO_x/Al_2O_3 and Ni-Mn_1O_x/Al_2O_3 catalysts*

To study the differences in the reaction mechanism between the non Ni-Mn MMO (NiO_x/Al_2O_3) and Ni-Mn MMO containing (Ni-Mn_1O_x/Al_2O_3) catalysts, the adsorbed and gaseous reaction species were identified with the aid of DRIFTS and semi-quantified by peak deconvolution. The accordant catalyst was deposited in the form of a coated layer onto a microstructured foil and investigated *operando* using a plate reactor [37] with optical access for DRIFTS. The gas phase is analyzed by gas chromatography (GC 8860, Agilent). The resulting spectra were processed as described in the experimental section.

Fig. 10 A) shows the time-resolved DRIFT spectra for the run-in behavior of the reaction at T = 100 °C with the NiO_x/Al_2O_3 catalyst. After recording the background spectra in nitrogen atmosphere, the reaction conditions ($CO_2/H_2/N_2$ = 1/4/5) were set. The clearly distinguishable peaks can be assigned to the various adsorbed species on the catalyst: tri- (2050–2080 cm^{-1}), di- (2045 cm^{-1}), and mono-carbonyls (2010 cm^{-1}) adsorb over a duration of one hour on the elemental nickel sites. Peaks that appear at 1926 cm^{-1} and 1838 cm^{-1} can be assigned to bridged and triple coordinated CO[15,38,39]. The spectra clearly show that the CO is adsorbed at active Ni sites and since only CO_2, H_2 and N_2 are used as feed gases, CO_2 must, thus, have been converted into adsorbed carbonyls at 100 °C. Two possible reaction pathways have been highlighted in literature. On one hand, CO_2 can dissociatively adsorb on the catalyst or via associative adsorption as carbonate (CO_2*) or bicarbonate (O-COOH*) [16,24,32,40]. Because no carbonate could be detected, the associative route seems to run exclusively via adsorption of bicarbonate. In addition to carbonyls, adsorbed bicarbonate (1649 cm^{-1}, 1440 cm^{-1} and 1230 cm^{-1}) and formate (O-COH*, 1580 cm^{-1}, 1630 cm^{-1}, 1330–1390 cm^{-1} and 2860 cm^{-1} see Figure S19) could also be identified [15,25,35,38,41,42]. In Fig. 10B), the time-resolved, normalized peak areas of the adsorbed species obtained by peak deconvolution are plotted over the time on stream during the run-in at T = 100 °C. Over time, an increasing amount of formate was detected on the catalyst surface which asymptotically approached a maximum after one hour. In contrast, bicarbonate adsorbed quickly at first, and after approximately 10 min, the surface concentration was reduced over time. It can be assumed that bicarbonate adsorbs first and then reacts further to form other species, namely formate. Linear and bridge-bound CO behaves similar to formate and asymptotically approaches a maximum over time.

Formate and CO continue to adsorb on the surface because at T = 100 °C, the reaction to CH_x molecules is not kinetically favored. It should be emphasized that according to the DRIFT spectra no CO_2 adsorbs on the catalyst, but either dissociates to CO* and O* and/or adsorbs as bicarbonate on the OH groups of the Al_2O_3 support.

After the run-in at 100 °C of the NiO_x/Al_2O_3 catalyst, the temperature was increased in 25 K steps up to 450 °C under reaction conditions with spectra being recorded at every 25 K step (Fig. 11 A). The carbonyl species (2010–2080 cm^{-1}, 1926 cm^{-1}, and 1838 cm^{-1}) decreased significantly with temperature. In particular, the tri-carbonyl desorbs almost completely up to 200 °C. The bicarbonate (O-COOH*, 1664 cm^{-1}, 1442 cm^{-1}, and 1226 cm^{-1}) completely disappeared from the surface at T = 150 °C and was converted into formate (O-COH*) and

Table 5
Methane formation rates, methane formation rates per g_{Ni} of the catalysts, CO_2 conversions and CH_4 selectivities at 350 °C and 1 bar for the reduced catalysts (15 wt% Ni) and comparison of this work (t.w.) with comparable catalytic systems reported in the literature. All methane formation rates were calculated using Eq. (7).

Catalyst	Methane formation rate r_{CH_4} at 350 °C [mol(CH_4) h^{-1} g_{cat}^{-1}]	Methane formation rate per $g_{Ni,cat}$ at 350 °C [mol(CH_4) h^{-1} $g_{Ni,cat}^{-1}$]	X (CO_2) [%]	S (CH_4) [%]	Ref.
NiO_x/Al_2O_3	0.14	1.0	7	51	t.w.
Ni-$Mn_{0.375}O_x$/Al_2O_3	0.78	5.3	21	85	t.w.
Ni-Mn_1O_x/Al_2O_3	0.58	4.2	18	75	t.w.
9 wt% Ni/ZrO_2-P	0.33	3.8	79	97	[34]
9 wt% Ni/Al_2O_3[a]	0.02	0.2	10	82	[35]
9 wt% Ni/CeO_2[a]	0.17	2.1	80	100	[35]
10 wt% Ni/Al_2O_3[a]	0.08	0.8	26	95	[24]
10 wt% NiFeK/Al_2O_3[a]	0.17	1.7	54	98	[24]
10 wt% Ni/MnO_x-NS	0.11	1.1	64	99	[28]
18 wt% Ni/Al_2O_3[a]	0.10	0.5	73	99	[16]
17 wt% Ni-Mn (0.25)/Al_2O_3[a]	0.11	0.6	80	100	[16]
3 wt% Ni-Mn (1:1)/TiO_2[a]	0.05	1.8	41	100	[15]
3 wt% Ni/TiO_2[a]	0.03	1.1	65	98	[15]

[a] calculated with values obtained from the catalytic performance diagrams.

CO*. The peak assigned to formate (1624 and 1591 cm^{-1}, 1392 and 1373 cm^{-1}) first increased with increasing temperature up to T = 175 °C and further lost almost all its intensity up to 450 °C. In Fig. 11 B), the normalized peak areas at representative wavenumbers of the adsorbed species and CH_4 (3014 cm^{-1}) are plotted vs. temperature between 100 and 450 °C showing that the amount of adsorbed bicarbonate and carbonyl species decreases rapidly, while the formate peak reaches a maximum at T = 175 °C, and CH_4 is formed starting from T = 250 °C and continues to increase until T = 450 °C. Over the whole experiment no adsorbed CO_2 could be found.

The Ni-Mn_1O_x/Al_2O_3 catalyst was also investigated using DRIFTS. Fig. 12 A) shows the time-resolved spectra recorded after switching from N_2 to the reaction gases at T = 100 °C. Initially, the concentration of all adsorbed species increased with time. The peaks of adsorbed CO, CO_2, and formate species approached saturation asymptotically over one hour, whereas the bicarbonate concentration drastically increased in the first three minutes and then gradually decreased over time until it nearly disappeared from the surface after 40 min. These trends can be seen more clearly when plotting the normalized peak areas for the representative peaks of the surface species vs. time on stream (Fig. 12 B). It can be seen that double-bound CO reached its maximum in the first ten minutes, whereas single-bound CO and formate steadily increased over the 60 min tested.

The bicarbonate concentration quickly reached a maximum and subsequently decreased again, which can be explained by the further reaction of bicarbonate to other species (e.g. formate). In this process, water is split off and formate remains bound to the surface.

The desorption of bicarbonate as a reason for the decrease in surface concentration can be excluded here, as adsorption experiments with CO_2 as feed did show that bicarbonate desorbs from the surface only at temperatures well above 100 °C (see Figure S18). These findings underline the hypothesis that, after the adsorption of CO_2 on the OH groups of the Al_2O_3 support as bicarbonate, this reacts further to formate by splitting off water. In addition to the OH groups, the manganese provides basic O^- groups at which CO_2 adsorbs as carbonate (CO_2*, 1523 and 1421 cm^{-1}) [15,28,38,40].

Fig. 13 A) shows the temperature-resolved spectra in the range between 100 and 450 °C of the Ni-Mn_1O_x/Al_2O_3 catalyst under reaction conditions. In comparison to the NiO_x/Al_2O_3 catalyst (see Fig. 11 A), there is no bicarbonate bound to the surface under stationary conditions, as this has already reacted to formate during the run-in (Fig. 12). Compared to the NiO_x/Al_2O_3 catalyst, the spectrum clearly shows that for the Ni-Mn_1O_x/Al_2O_3 catalyst the carbonyl concentration is way lower in relation to the formate concentration. Already at 100 °C, the carbonyls concentration on the Ni-Mn_1O_x/Al_2O_3 catalyst surface is comparably low, and it further decreases with temperature and almost disappeared at 250 °C (Fig. 13 B). Monodentate carbonate and formate show a similar trend, with both exhibiting a rather constant concentration up to 200 °C before both steadily decrease. As the concentration of the intermediate species decreased, methane was detected via DRIFTS

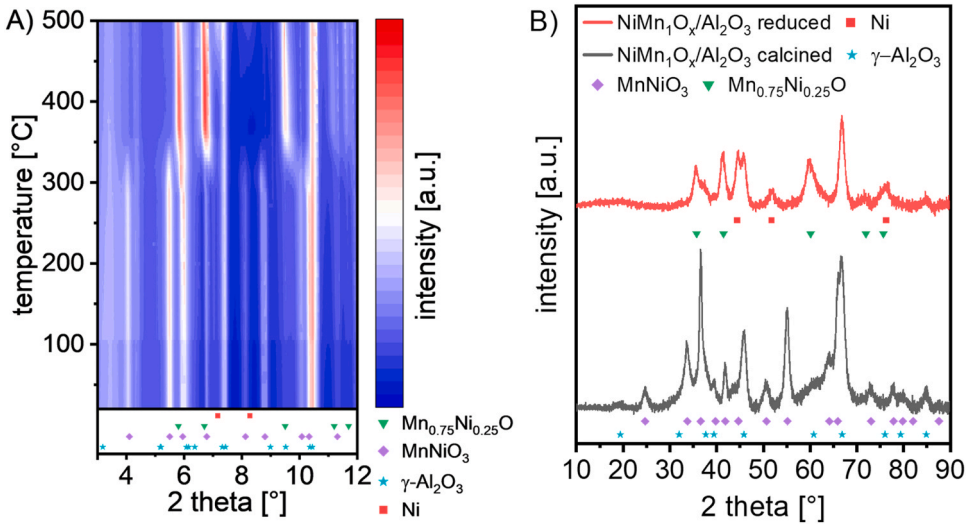

Fig. 5. A) *In situ* TPR-XRD measurements of Ni-Mn_1O_x/Al_2O_3. Conditions: 10 % H_2 in He with a flow rate of 16 ml min^{-1}, Ramp: 10 K min^{-1}. B) *Ex situ* XRD of calcined and reduced Ni-Mn_1O_x/Al_2O_3, reduction conditions: 5 % H_2 in N_2 at 450 °C for 1 h.

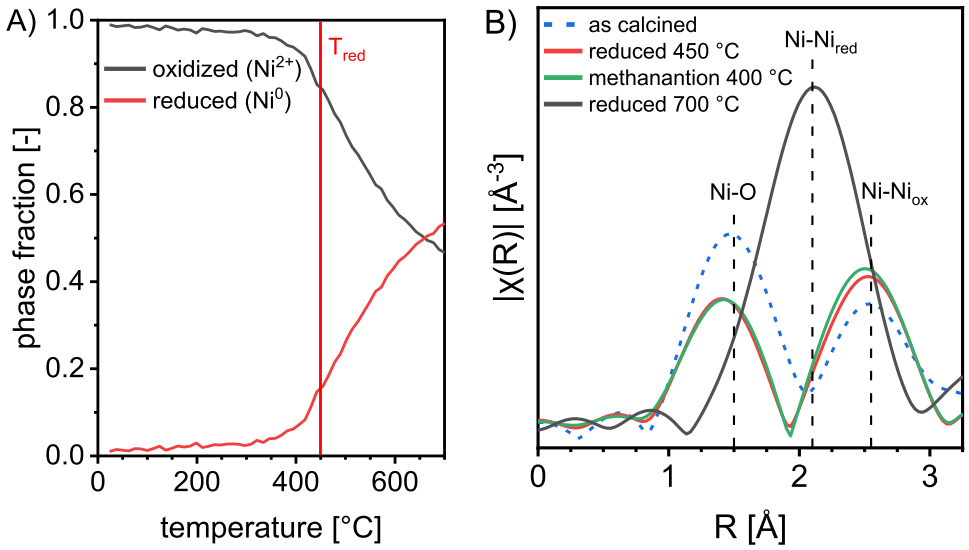

Fig. 6. A) LCF of the Ni K-edge of the *in situ* TPR-XAS measurement of Ni-Mn_1O_x/Al_2O_3. Conditions: 10 % H_2 in He with a flow rate of 16 ml min^{-1}, Ramp: 10 K min^{-1}. B) Ni K-edge Fourier-transformed k^3-weighted EXAFS spectra of the different reduction states of Ni-Mn_1O_x/Al_2O_3.The measurement of the calcined and reduced 700 °C sample were taken at room temperature, the other samples were measured at the temperature indicated in the figure. Conditions: Pretreatment: 10 % H_2 in He at 450 °C for 1 h, methanation: c(CO_2) = 6.25 vol%, CO_2/H_2 = 1/4 diluted in He, total flow rate: 16 ml min^{-1}, GHSV = 127270 h^{-1} and p = 1 bar.

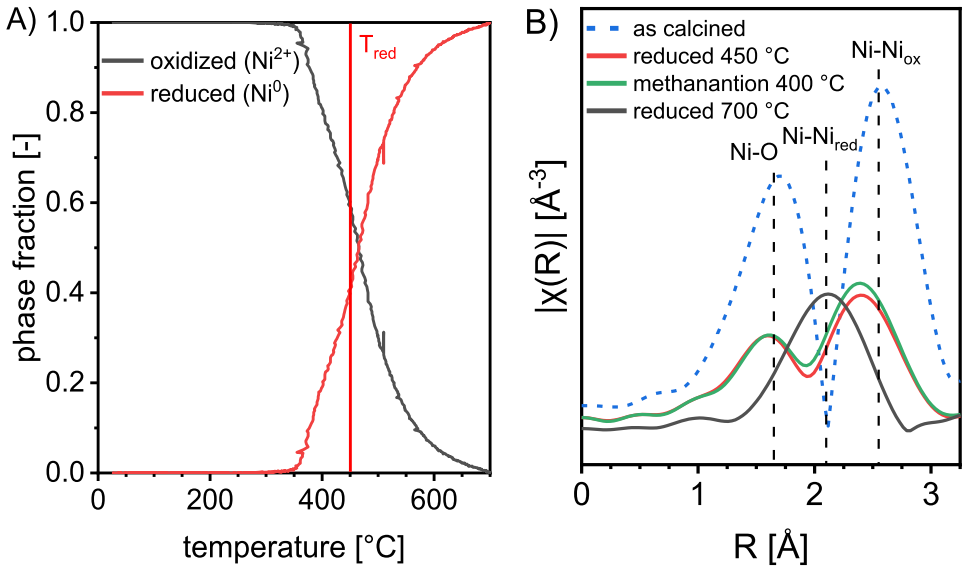

Fig. 7. A) LCF of the Ni K-edge of the *in situ* TPR-XAS measurement of NiO_x/Al_2O_3. Conditions: 10 % H_2 in Ar with a flow rate of 16 ml min^{-1}, Ramp: 8 K min^{-1}. B) Ni K-edge Fourier-transformed k^3-weighted EXAFS spectra of the different reduction states of NiO_x/Al_2O_3. The measurement of the calcined sample was taken at room temperature, the other samples were measured at the temperature indicated in the figure. Conditions: pretreatment: 10 % H_2 in Ar at 450 °C for 1 h, methanation: c(CO_2) = 6.25 vol%, CO_2/H_2 = 1/4 diluted in Ar, total flow rate: 16 ml min^{-1}, GHSV = 127270 h^{-1} and p = 1 bar.

and in the product gas (online gas chromatograph, results not shown).

2.5. Reaction mechanism

Depending on the catalyst system, two pathways have been proposed in the literature, in which formate is either involved in the reaction as an intermediate or only plays a spectator role. Many authors assume that formate serves as an intermediate and is then either directly hydrogenated to methane or first hydrogenated to CO* with subsequent hydrogenation to methane[10,14,23–25,28,33,35,40,43]. Formate can be formed via carbonates or bicarbonates [26].

Our *operando* DIRFTS analysis reveals that a major difference in the reaction mechanism on the Ni-Mn MMO can be caused by the carbonate, which is bound to the catalyst surface. In contrast to the NiO_x/Al_2O_3 catalyst, CO_2 adsorbs not only as bicarbonate on the hydroxyl groups but also on the Ni-Mn MMO to form carbonate. Tentative reaction mechanisms for the two catalyst systems investigated in this study, namely NiO_x/Al_2O_3 and Ni-Mn_1O_x/Al_2O_3, can be deduced from the adsorbed surface species determined via *operando* DRIFTS data. Combining the findings reported and discussed above, for the NiO_x/Al_2O_3 catalyst the CO_2 methanation mechanism depicted in Fig. 14 A) is proposed. The NiO_x/Al_2O_3 catalyst is rich in surface OH groups to which CO_2 is adsorbed in the form of bicarbonate (Fig. 14, step I). The hydrogen is exclusively activated on the Ni^0 nanoparticle by dissociative adsorption (Fig. 14, step I) and then reacts further with bicarbonate to formate (step II) and splits off water. In addition to bicarbonate, CO_2 adsorbs dissociatively as carbonyl and oxygen on the nickel sites (step III), and the oxygen reacts further with hydrogen to form water (step V). Moreover, a

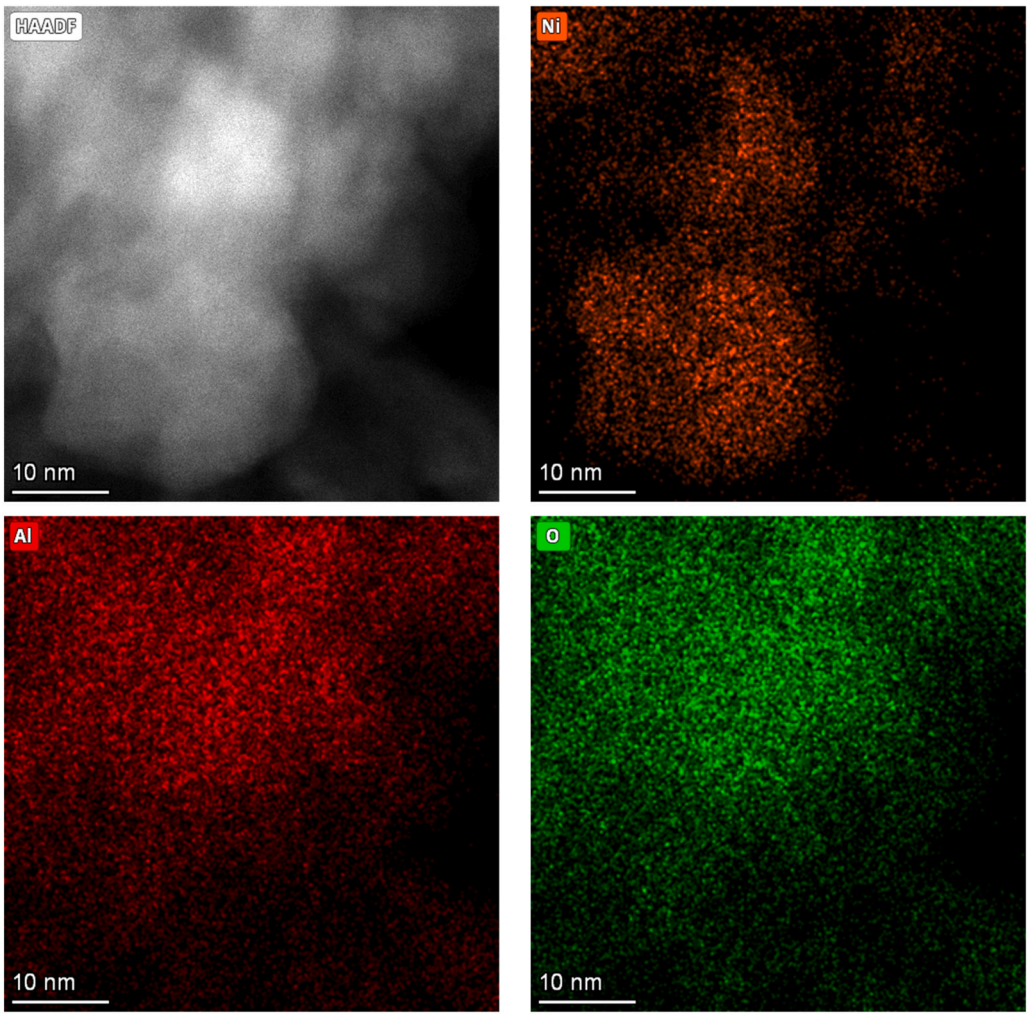

Fig. 8. High-angle annular dark field scanning transmission electron microscopy (HAADF-STEM) and energy-dispersive X-ray (EDX) spectrum imaging of reduced NiO_x/Al_2O_3 catalyst, reduction conditions: 5 % H_2 in N_2 at 450 °C for 1 h.

carbonyl can also be formed when formate decomposes to form an OH group on the Al_2O_3 support and a carbonyl on the Ni sites (step IV), which can react with hydrogen to form methane and water (step VI and VII). In addition to CO methanation, formate can also react directly with hydrogen and split off water to eventually form methane (steps VIII, IX and X). The fact that no carbonate could be detected on the NiO_x/Al_2O_3 catalyst using DRIFTS rules out the reaction pathways with adsorbed carbonate as the starting point. The proposed mechanism is in line with the literature, although depending on the catalyst system, the focus is sometimes only on the CO*- or the formate-mediated pathway[15, 23–26,33,40,43]. An extended scheme of the CO_2 methanation reaction mechanism for the Ni-Mn_1O_x/Al_2O_3 catalyst is shown in Fig. 14 B). Similar to the NiO_x/Al_2O_3 catalyst, CO_2 can adsorb dissociatively on the Ni^0 sites of the Ni-Mn MMO catalyst or on the OH groups of Al_2O_3. Additionally, the Ni-Mn mixed oxide offers sites to adsorbs CO_2 as carbonates (step XI). Furthermore, the reducible Ni-Mn MMO phase can provide defects/oxygen vacancies that can also be active for CO_2 adsorption and activation (step XIII). Formate is most likely only present on basic sites and not on Ni^0 nanoparticles. These two ways of CO_2 adsorption have already been reported for various catalytic systems [25–29,43]. The adsorbed CO_2 then reacts further with hydrogen to first form formate (step XII and XIV) before following the reaction pathways shown in Fig. 14 A) to form methane.

According to the tentative reaction mechanism, CO can be formed as a by-product either by desorption from the CO*-mediated reaction pathway or by dissociative CO_2 adsorption. For the Ni-Mn MMO catalysts, it is possible that dissociative CO_2 adsorption occurs on the reducible Ni-Mn MMO phase involving defects/oxygen vacancies (redox cycle), as described by Aldana et al. for Ni ceria-zirconia catalysts [43]. Dissociative adsorption of CO_2 on Ni^0, which according to Schmider et al. has an activation energy of 89.3 kJ mol^{-1}, is most likely less favored for the Ni-Mn MMO catalyst [32]. This is evident in the differences in the Ni specific methane formation rates and apparent activation energies of the Ni-Mn MMO and non Ni-Mn MMO containing catalysts (see Table 4). Due to the high CO_2 adsorption capacity, the proximity of basic sites and active Ni sites in the Ni-Mn MMO catalysts, we propose that the CO*-mediated reaction pathways lead to undesired CO formation (Fig. 14 B). This is in line with observations on NiO_x/Al_2O_3. Herein the direct hydrogenation of formate is not the only reaction path. Significant quantities of CO are formed as by-product, yielding in lower CH_4 selectivity, thus the reaction is more likely to take place via the CO*-mediated reaction pathways (steps IV, VI and VII).

3. Conclusion

In contrast to previous studies, in which manganese was used as a promoter in smaller quantities [14–16,18,19], we opted for a higher Mn content, up to 14 wt% Mn (Mn/Ni ratio of 1), to obtain a supported Ni-Mn mixed-metal oxide phase with unique properties. The addition of manganese increased the number of weak basic sites, as well as the

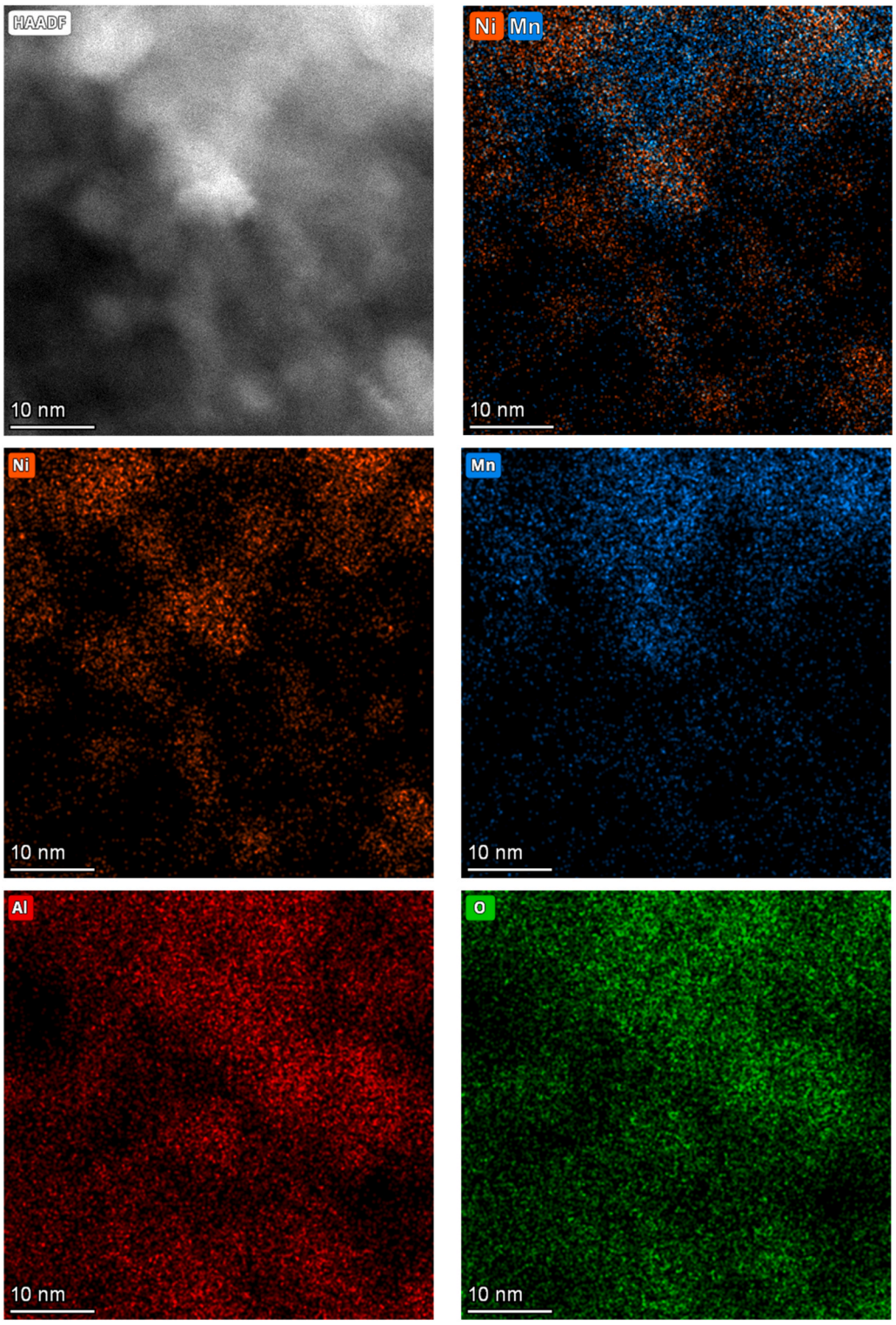

Fig. 9. HAADF-STEM and EDX spectrum imaging of reduced Ni-Mn_1O_x/Al_2O_3 catalyst, reduction conditions: 5 % H_2 in N_2 at 450 °C for 1 h.

active Ni surface area, compared to the literature-based state-of-the-art type NiO_x/Al_2O_3 catalyst. The catalytic results shown here demonstrate that the supported Ni-Mn MMO catalysts are highly active and selective in CO_2 methanation under the conditions applied. All supported Ni-Mn MMO containing catalysts exhibited similarly high Ni-specific methane formation rates and yields, outperforming the NiO_x/Al_2O_3 reference catalysts by approximately 31 %. In addition, they achieved at least three times higher methane formation rates. The differences in catalytic performance between the NiO_x/Al_2O_3 and Ni-Mn MMO catalysts cannot be solely attributed to the differences in Ni surface area. This indicates that the Ni-Mn MMO phase contributes to the catalytic activity. This was also supported by the Ni-$Mn_{0.125}O_x/Al_2O_3$ catalyst, which, even though it had the largest Ni surface area of all the catalysts tested, did not show the best catalytic performance and had a Ni specific methane formation rate similar to that of the NiO_x/Al_2O_3 catalyst. In contrast, the variations in performance among the different Ni-Mn MMO catalysts can be

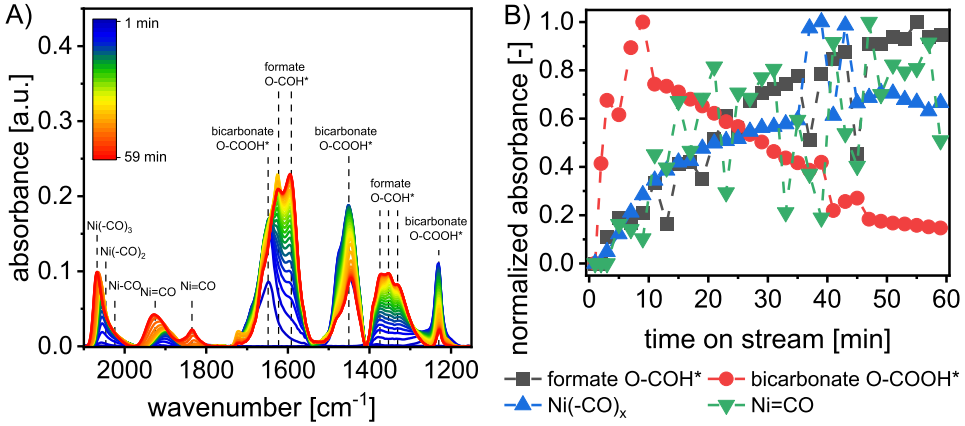

Fig. 10. A) Time-resolved DRIFT spectra ($\Delta t = 2$ min for $t > 3$ min, $\Delta t = 1$ min for t 0–3 min) for the NiO_x/Al_2O_3 catalyst at p = 5 bar, $CO_2/H_2/N_2 = 1/4/5$, SV = 4.6 $ml_N\ mg_{cat}^{-1}\ min^{-1}$ and T = [1]00 °C. B) Time-resolved normalized absorbance of the peak areas for formate (1373 cm^{-1}), bicarbonate (1439 cm^{-1}), Ni-CO ([2]069 cm^{-1}) and Ni=CO (1926 cm^{-1}).

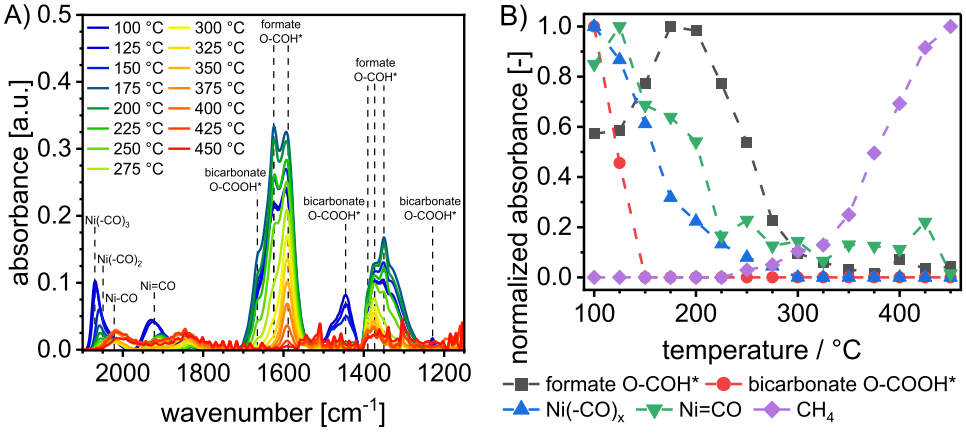

Fig. 11. A) Temperature-resolved DRIFT spectra for the NiO_x/Al_2O_3 catalyst at 5 bar, $CO_2/H_2/N_2 = 1/4/5$, SV = 4.6 $ml_N\ mg_{cat}^{-1}\ min^{-1}$. B) Temperature-resolved, normalized absorbance of the peak areas for formate (1373 cm^{-1}), bicarbonate (1439 cm^{-1}), Ni-CO (2069 cm^{-1}), Ni=CO (1926 cm^{-1}) and CH_4 (3014 cm^{-1} not shown).

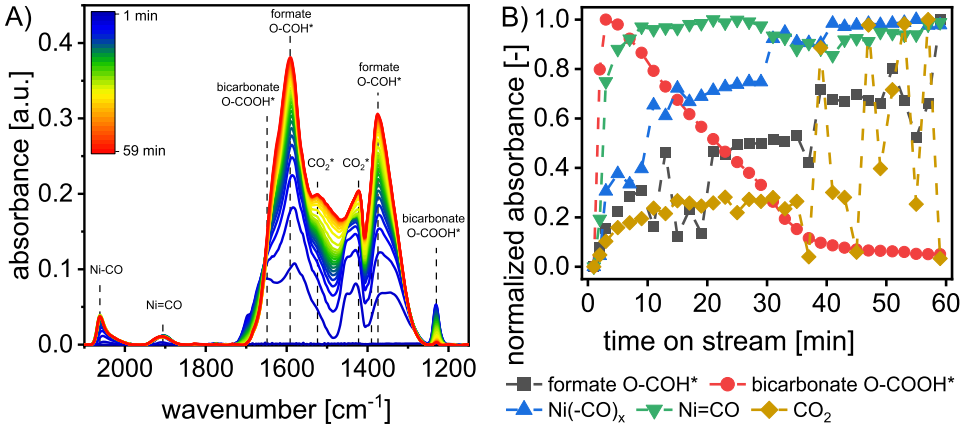

Fig. 12. A) Time-resolved DRIFT spectra ($\Delta t = 2$ min for $t > 3$ min, $\Delta t = 1$ min for t 0–3 min) for the Ni-Mn_1O_x/Al_2O_3 catalyst at p = 5 bar, $CO_2/H_2/N_2 = 1/4/5$, SV = 4.6 $ml_N\ mg_{cat}^{-1}\ min^{-1}$ and T = [1]00 °C. B) Time-resolved normalized absorbance of the peak areas for formate (1373 cm^{-1}), bicarbonate (1439 cm^{-1}), Ni-CO (2069 cm^{-1}), Ni=CO ([1]926 cm^{-1}) and CO_2* (1425 cm^{-1}).

ascribed to differences in their Ni surface area (see Table 2, Table 4 and Fig. 4). Therefore, Ni-Mn_1O_x/Al_2O_3 was selected for further investigations as it contains the largest amount of the $MnNiO_3$ MMO phase.

In situ XAS and XRD measurements as well as *ex situ* STEM were used to investigate the differences in the activation behavior of the state-of-the-art type supported catalyst (NiO_x/Al_2O_3) and the novel supported Ni-Mn mixed metal oxide catalyst (Ni-Mn_1O_x/Al_2O_3) catalysts. It was

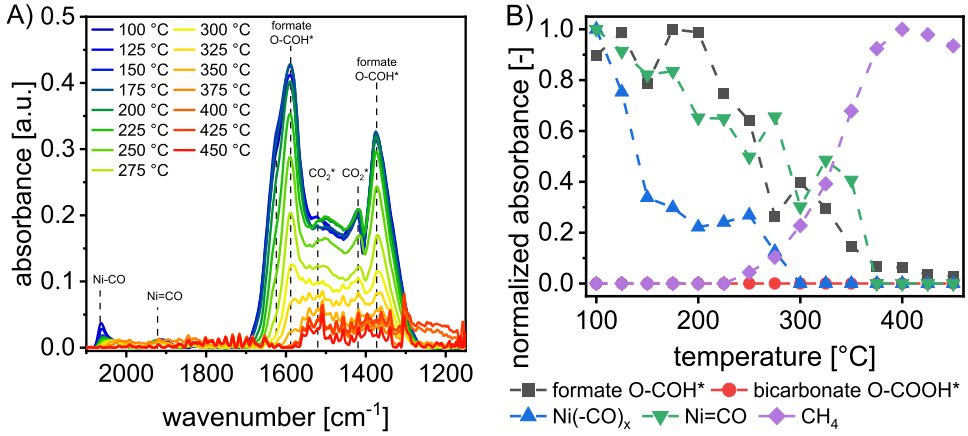

Fig. 13. A) Temperature-resolved DRIFT spectra for the Ni-Mn_1O_x/Al_2O_3 catalyst at 5 bar, $CO_2/H_2/N_2 = 1/4/5$, SV = 4.6 $ml_N\ mg_{cat}^{-1}\ min^{-1}$. B) Temperature-resolved normalized absorbance of the peak areas for formate (1373 cm^{-1}), bicarbonate (1439 cm^{-1}), Ni-CO (2069 cm^{-1}), Ni=CO (1926 cm^{-1}) and CH_4 (3014 cm^{-1} not shown).

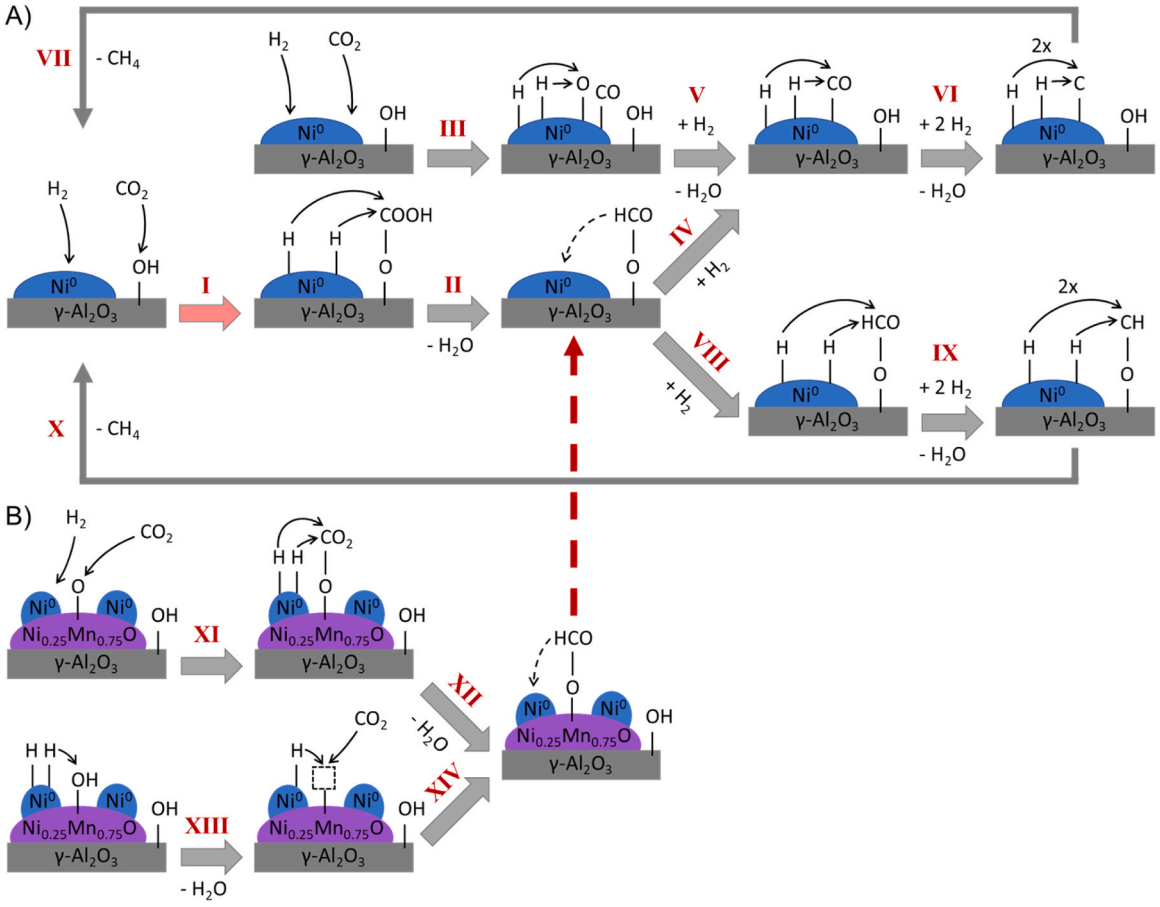

Fig. 14. A) Proposed reaction mechanism for the NiO_x/Al_2O_3 catalyst. (I) Associative adsorption of CO_2 on the Hydroxyl groups of the carrier. (III and V) Dissociative adsorption of CO_2 onto active Ni sites with consecutive water formation. (II) Hydrogenation of bicarbonate to formate. (IV, VI and VII) Dissociation of formate to CO and OH with consecutive hydrogenation of CO to CH_4 (VIII, IX and X) Hydrogenation of formate to methane. B) Proposed extended reaction mechanism for the Ni-Mn_1O_x/Al_2O_3 catalyst. (XI) CO_2 adsorption as carbonate on the $Ni_{0.25}Mn_{0.75}O$ interface. (XIII) CO_2 adsorption in defects/oxygen vacancies (□). (XII and XIV) Successive hydrogenation to formate.

found that for the Ni-Mn MMO catalyst, upon activation, the $MnNiO_3$ phase was reduced to a Ni-depleted $Mn_{0.75}Ni_{0.25}O$ MMO phase resulting in finely dispersed Ni nanoparticles on top of this supported Ni-Mn MMO phase. All the catalysts tested showed no significant loss in catalytic performance under the reaction conditions and time on stream tested. For further mechanistic investigation, *operando* DRIFTS measurements were performed, and from the data obtained a reaction scheme with CO*- and formate-mediated pathways was developed for NiO_x/Al_2O_3 and extended for the Ni-Mn_1O_x/Al_2O_3 catalyst (Fig. 14). The data presented show that the NiO_x/Al_2O_3 catalyses the CO_2 methanation reaction via a coupled CO* and formate reaction mechanism, excluding any carbonate intermediates. However, the formation of the reducible Ni-

Mn MMO phase leads to an increase in the number of weak basic sites, resulting in the formation of carbonate intermediates. Furthermore, the formation of defects/oxygen vacancies in this catalyst system opens up an additional pathway for CO_2 activation (see Fig. 14 B). This difference in the proposed mechanisms is supported by the decrease in the apparent activation energy with increasing Mn content and the significant difference in the Ni specific methane formation rates between the non Ni-Mn MMO-containing (NiO_x/Al_2O_3 and $Ni\text{-}Mn_{0.125}O_x/Al_2O_3$) and the Ni-Mn MMO-containing catalysts (Mn/Ni ratio $\geq$ 0.375).

In summary, we have shown that the addition of high Mn contents and thus high Mn/Ni ratios (> 5 wt%) leads to a novel supported Ni-Mn MMO catalyst that exhibits differences in activation and reaction mechanism compared to the self-synthesized, literature based state-of-the-art type NiO_x/Al_2O_3 catalyst. This leads to a significant increase in the methane formation rates, also in comparison to other catalysts reported in the literature (see Table 5).

4. Experimental section

4.1. Catalyst preparation

$Ni\text{-}Mn_yO_x/Al_2O_3$ ($0 \leq x \leq 2$) catalysts were prepared by incipient wetness impregnation of the corresponding nitrates with the Al_2O_3 support (Puralox TH 100/150 from Sasol). For this the appropriate amounts of $Ni(NO_3)_2 \bullet 6\ H_2O$ (Thermo scientific, 99 %) and $Mn(NO_3)_2 \bullet 4\ H_2O$ (Alfa Aesar, 98 %) were dissolved in deionized water and slowly added to the support. The catalyst was dried overnight at 75 °C and calcined in air at 500 °C for 6 h with a heating ramp of 5 K min^{-1}.

4.2. Catalyst characterization

4.2.1. X-ray powder diffraction

X-ray powder diffraction of the catalysts was studied using a Philips X'Perts X-ray diffractometer using Cu Kα radiation at an angle of 10° to 90° with a step size of 0.017° and 100 s per step. $MnNiO_3$/NiO phase ratio was estimated using the semi-quantitative reference intensity ratio (RIR) method in the HighScore Plus software[30]. Only the references for $MnNiO_3$ and NiO were used to illustrate the trend of the phase ratio at different Mn content, and Al_2O_3 was omitted. This method uses the measured diffraction intensity and the RIR values of the specified reference phases to calculate the estimated mass fraction according to Eq. 2.

$$X_a = \frac{I_{(hkl)a}}{RIR_a \quad I^{rel}_{(hkl)a}} \left[\frac{1}{\sum_{j=1}^{\#phases} \left(\frac{I(hkl)_j}{RIR_j \quad I^{rel}_{(hkl)_j}} \right)} \right] \tag{2}$$

4.2.2. N_2 physisorption

The specific surface areas (S_{BET}) and pore volume were determined by N_2 physisorption in a Quantachrome QuadraSorb SI using the Quadrawin™ software. The total pore volume was determined at $p/p_0 \geq 0.99$ and the specific surface area with the Brunauer-Emmett-Teller method at $p/p_0 = 0.05 - 0.21$. Prior to sorption measurements, the samples were degassed at 200 °C for 12 h in vacuum.

4.2.3. Temperature programmed reduction

The AutoChem II & HP from Micromeritics was used for temperature programmed reduction. After purging in Ar at 450 °C for 0.5 h and cooling, the samples were heated to 950 °C with a ramp of 5 K min^{-1} in 10 % H_2 in Ar. All steps were carried out at a flow rate of 50 ml min^{-1}.

4.2.4. Temperature programmed desorption

Temperature programmed desorption of CO_2 was performed using a AutoChem II & HP from Micromeritics. Pretreatment was carried out in 10 % H_2 in Ar with a flow rate of 50 ml min^{-1} at 450 °C for 1 h. All subsequent steps were carried out at a flow rate of 20 ml min^{-1}. After purging for 0.5 h and cooling in He, pure CO_2 was adsorbed at 100 °C for 1 h, followed by a 1 h purge with He. CO_2-TPD was carried out in He with a ramp of 5 K min^{-1} up to 800 °C.

4.2.5. Inductively coupled plasma atomic emission spectroscopy (ICP-AES)

The composition of the synthesized catalysts was determined by elemental analysis using inductively coupled plasma atomic emission spectroscopy (ICP-AES) with a SPECTRO Ciros CCD.

4.2.6. N_2O titration

The AutoChem II & HP from Micromeritics was used for N_2O titration. Pretreatment was carried out in 10 % H_2 in Ar with a flow rate of 50 ml min^{-1} at 450 °C for 1 h, which corresponds to the pretreatment conditions in the catalytic experiments. The sample is then purged at 500 °C for 0.5 h in He. N_2O titration is performed by passing 40 ml min^{-1} 0.5 % N_2O in He over the sample and measuring the resulting nitrogen according to the reaction 3 with a thermal conductivity detector. The excess N_2O is removed in a cold trap with liquid nitrogen. The active nickel surface area is estimated using Eq. 4, where n_{N2} is the amount of N_2 produced (mol), N_A is the Avogadro constant, S_{Ni} is the number of Ni surface atoms per unit area ($1.54 \bullet 10^{19}$ m^{-2}), m_{cat} is the amount of catalyst used, ω_{Ni} is the Ni loading and ρ_{Ni} is the Ni density (8.91 g cm^{-3}) [31].

$$Ni + N_2O \rightarrow NiO + N_2 \tag{3}$$

$$A_{Ni} = \frac{n_{N2} \bullet N_A}{S_{Ni}} \tag{4}$$

$$A_{Ni,norm} = \frac{A_{Ni}}{m_{cat}} \tag{5}$$

4.2.7. High-angle annular dark field scanning transmission electron microscopy (HAADF-STEM) and energy-dispersive X-ray spectroscopy (EDXS)

High-angle annular dark field scanning transmission electron microscopy (HAADF-STEM) was used for the estimation of the metal distribution and the nanoparticle size of the reduced catalysts, in conjunction with energy-dispersive X-ray spectroscopy (EDXS). The work was carried out using a Talos F200i (ThermoFisher Scientific) with an acceleration voltage of 200 kV. Remote air plasma cleaning was performed using a Tergeo-EM plasma cleaner (PIE Scientific) to remove adsorbed hydrocarbons and thus reduce carbon deposition during imaging.

4.3. Catalytic testing

4.3.1. Methanation experiments

Catalytic experiments were performed in a fixed-bed reactor with a diameter of 10 mm at ambient pressure. For each experiment, 0.02 g of 100–150 µm catalyst was used and diluted in 2.5 g of 200–300 µm quartz sand. Pretreatment was carried out at 450 °C in 10 % H_2 in Ar for 1 h, followed by a run-in period of 6 h at 450 °C under methanation conditions. The CO_2 methanation was performed with a H_2/CO_2 ratio of 4/1 diluted in 68.75 % Ar, a total flow rate of 523.6 ml min^{-1} resulting in a gas hourly space velocity (GHSV) of 20,000 h^{-1}. The temperature was changed from 250 to 450 °C in 25 K increments. The gas flow was controlled with mass flow controllers (Bronkhorst EL-Flow), and the relative concentrations of the product gases were analyzed with a Pfeiffer Vacuum OmniStar GSD 350 mass spectrometer. The only by-product detected was CO. Therefore, the CO_2 conversion (4), CH_4 selectivity (5), CH_4 yield (6) and methane formation rate (7) were calculated using the following equations. The apparent activation energies were calculated in a CO_2 conversion range of 3.5–11 % from the

average of either two cycles (C1 & 2) with the same catalyst or two experiments (E1 & 2) using the Arrhenius equation (see Figure S20). The standard deviation of three to four experiments was 0.5–2 kJ mol^{-1} for the catalysts tested. For reasons of clarity, only two measurements were plotted in Figure S20. The maximum deviation of 2 kJ mol^{-1} was used as the error.

$$X(CO_2) = \frac{(n_{CO_2\,in} - n_{CO_2\,out})}{n_{CO_2\,in}} \bullet 100\% \quad (4)$$

$$S(CH_4) = \frac{(n_{CH_4\,out} - n_{CH_4\,in})}{(n_{CH_4\,out} - n_{CH_4\,in}) + (n_{CO\,out} - n_{CO_{in}})} \bullet 100\% \quad (5)$$

$$Y(CH_4) = X(CO_2) \bullet S(CH_4) \quad (6)$$

$$r_{CH_4} = \frac{\dot{V}_{CO_2,in} \bullet Y(CH_4) \bullet p_N}{R \bullet T_N \bullet m_{cat}} \quad (7)$$

4.3.2. Operando DRIFTS measurements

Adsorbed species on the catalysts surface have been tracked via diffuse reflectance infrared Fourier-transform spectroscopy (DRIFTS). Many species that participate in the methanation reaction absorb infrared radiation and can therefore be visualized in a spectrogram. The DRIFTS investigations were carried out at the Institute of Micro Process Engineering of the Karlsruhe Institute of Technology. The radiation source used was a Bruker IR cube FT-IR OEM spectrometer with an MCT detector cooled with liquid nitrogen. The reactor used was a slightly modified version of the reactor described by Engl et al. [37] The spectrograms were recorded with a spectral resolution of 4 cm^{-1} and averaged over 40 spectra. In order to be able to compare the results of the different catalysts, all experiments were carried out using the same procedure. The catalysts were heated to 450 °C in a nitrogen atmosphere with a ramp of 100 K h^{-1} and then reduced in 10 % hydrogen for 1 h. After switching back to inert gas and purging with nitrogen for half an hour, the temperature was cooled from 450 to 100 °C in 25 K steps. Background spectra were recorded after constant temperatures were reached at each step. At 100 °C, the gas inlet was changed from nitrogen atmosphere to reaction conditions (space velocity (SV) = 4.6 $ml_N\ mg_{cat}^{-1}\ h^{-1}$, $CO_2/H_2/N_2$ = 1/4/5, p = 5 bar). After taking a spectrum every minute during run-in, equilibrium was reached after approx. 1 h. The temperature was then increased to 450 °C in 25 K steps, and a spectrum was recorded after 15 min at each step. The resulting spectra were first subjected to baseline correction and then the individual peaks were fitted to a Gaussian function using Origin software via peak deconvolution. The resulting peak areas were plotted for each species and thus semi-quantified.

4.3.3. Operando X-ray absorption measurements

4.3.3.1. Sample preparation and operando conditions. The catalysts were tested using the quartz capillary flow reactor cells (1 mm OD) and gas delivery systems available at the beamlines. The corresponding catalysts were either undiluted (PSI) or diluted 1:3 with quartz (ESRF), pressed, crushed, and the 50–100 μm fraction was filled into the capillaries. Depending on the experiment, the following procedures were used. The temperature programmed reductions (TPR) were conducted in 10 % H_2 in He/Ar, with a heating ramp of 8–10 K min^{-1} up to 900 °C. Pretreatment/Reduction of the catalyst was carried out by heating to 450 °C and holding for 1 h in 10 % H_2 in He/Ar. The *operando* CO_2 methanation experiments were carried out at ambient pressure and 400 & 450 °C with $c(CO_2)$ = 6.25 vol%, $c(H_2)$ = 25 vol% in He/Ar and a GHSV of 127,270 h^{-1}. Due to the vast differences in intensity in the *operando* experiments of the manganese-containing and free catalysts, which are probably due to the different dilutions of these catalysts, the FT-EXAFS spectra are only compared qualitatively, and no EXAFS fits are done (see Figure S10). The intensity of the samples measured as pellets is comparable (see Figure S10b).

4.3.3.2. NiO_x/Al_2O_3 results. Operando Ni K-edge (8120 – 9120 eV) X-ray absorption spectra were measured at the SuperXAS beamline of the Swiss Light Source (SLS) at the Paul Scherrer Institute. The incident X-ray beam was collimated using a Si-coated mirror set at 2.9 mrad prior to monochromatization with a liquid nitrogen-cooled, channel-cut Si(111) crystal. Subsequently, the monochromatic beam was focused using a Rh-coated toroidal double-focusing mirror, resulting in a beam size of 0.7 mm (horizontal) by 0.2 mm (vertical). Moreover a 15 cm ionization chamber filled with 1 bar of N_2 was used. Quick fluorescence detection was carried out using a PIPS detector. The monochromator was oscillated at a frequency of 2 Hz, providing a time resolution of 0.5 s per spectrum. Energy calibration and linear combination fitting were performed using the ProXAS software [44], with calibration referenced to a simultaneously measured Ni foil. Linear combination fitting of the XANES region was executed using spectra from the fully reduced Ni/Al_2O_3 catalyst and the fully oxidized NiO/Al_2O_3 catalyst. EXAFS data processing was carried out with the Demeter software package (Athena) [45].

4.3.3.3. $Ni\text{-}Mn_1O_x/Al_2O_3$ results. Quasi-simultaneous XRD and XAS data were collected in transmission mode for Ni and in fluorescence mode for Mn at BM31 beamline of the European Synchrotron Radiation Facility (ESRF). Ni & Mn K-edges were measured in the XANES (for Ni: 8270–8430 eV, Mn: 6500–6650 eV) or EXASF (for Ni: 8230–9330 eV, Mn: 6440–7540 eV) range depending on the experiment. The Mn-EXAFS and the Ni-EXAFS for the TPR experiments were taken before and after the experiments at room temperature, averaging multiple scans due to the low signal intensity (Mn) or time sensitivity of the TPR measurements. In addition, Debye-Scherrer rings were recorded (energy: 48.6 keV, wavelength: 0.25509 Å) and 1D XRD patterns in the range 1–19.5° 2θ were obtained after ring integration to follow phase transitions during the experiments. In transmission mode three ionization chambers were used. Considering scan time and motors movements, the collection of a single XAS/XRD data for both K-edges took about 6.5 min. Linear combination fitting of the XANES region was executed with the ProXAS software [44] using Ni spectra from the fully reduced Ni/Al_2O_3 catalyst and the fully oxidized $Ni\text{-}Mn_1O_x/Al_2O_3$ catalyst. For the Mn spectra, the oxidized and the fully reduced $Ni\text{-}Mn_1O_x/Al_2O_3$ were used as references, as their pre-edge and shape match the corresponding MnO_2 and MnO pellet references (see Figure S1). To visualize the phase changes in the XRD data more clearly, the quartz reflections were masked using the reflex positions of quartz low (98–008–9280) and quartz high (98–008–9288) and the temperature-dependent linear combinations of the two phases (Fig. 5 and Figure S21). The EXAFS data was processed with Athena [45].

CRediT authorship contribution statement

Tanja Franken: Writing – review & editing, Validation, Supervision, Project administration, Methodology, Funding acquisition, Conceptualization. **Michael Rubin:** Writing – review & editing, Supervision, Project administration, Methodology, Funding acquisition, Conceptualization. **Roland Dittmeyer:** Writing – review & editing, Supervision. **Malte Raabe:** Validation, Investigation. **Andreas Hutzler:** Visualization, Validation, Investigation. **Dennis Weber:** Writing – original draft, Validation, Methodology, Investigation, Formal analysis, Data curation, Conceptualization. **Timo Engl:** Writing – original draft, Visualization, Validation, Investigation, Conceptualization.

Declaration of Competing Interest

The authors declare that they have no known competing financial interests or personal relationships that could have appeared to influence

the work reported in this paper.

Acknowledgements

The authors kindly acknowledge funding by the German Research Foundation (DFG, FR 3856/2–2 and KL 3223/1–1 and −2) in the framework of the priority program SPP2080 „DynaKat - Catalysts and reactors under dynamic conditions for energy storage and conversion“. Tanja Franken additional acknowledges the funding by the SPP2080 “DynaKat” Early Career Research Scholarship for female scientists and by the Cluster of Excellence Engineering of Advanced Materials through the EAM Starting Grant. The authors also kindly acknowledge support of the SuperXAS beamline of the Swiss Light Source in PSI and the Swiss Norwegian beamline BM31 in ESRF. The BM31 setup was funded by the Swiss National Science Foundation (grant 206021_189629) and the Research Council of Norway (grant 296087). We would also like to thank Lorena Baumgarten (KIT-ITCP, Grunwaldt group) and David Kellermann (TU Dortmund, REC, Freund group) for their help during the beamtime and the fruitful discussions.

Appendix A. Supporting information

Supplementary data associated with this article can be found in the online version at doi:10.1016/j.apcata.2025.120582.

Data availability

All data included in this manuscript are accessible via this DOI: https://doi.org/10.5281/zenodo.15064565

References

[1] S.V. Krupa, R.N. Kickert, The greenhouse effect: impacts of ultraviolet-b (uv-b) radiation, carbon dioxide (Co_2), and ozone (O_3) on vegetation, Environ. Pollut. 61 (1989) 263, https://doi.org/10.1016/0269-7491(89)90166-8.
[2] M. Meinshausen, S.J. Smith, K. Calvin, J.S. Daniel, M.L.T. Kainuma, J.-F. Lamarque, K. Matsumoto, S.A. Montzka, S.C.B. Raper, K. Riahi, et al., The RCP greenhouse gas concentrations and their extensions from 1765 to 2300, Clim. Change 109 (2011) 213, https://doi.org/10.1007/s10584-011-0156-z.
[3] P. Sabatier, New synthesis of methane, Comptes Rendus 134 (1902) 514.
[4] M. Götz, J. Lefebvre, F. Mörs, A. McDaniel Koch, F. Graf, S. Bajohr, R. Reimert, T. Kolb, Renewable power-to-gas: a technological and economic review, Renew. Energy 85 (2016) 1371, https://doi.org/10.1016/j.renene.2015.07.066.
[5] M. Bailera, P. Lisbona, L.M. Romeo, S. Espatolero, Power to gas projects review: lab, pilot and demo plants for storing renewable energy and co_2, Renew. Sustain. Energy Rev. 69 (2017) 292, https://doi.org/10.1016/j.rser.2016.11.130.
[6] M. Specht, J. Brellochs, V. Frick, B. Stürmer, U. Zuberbühler, M. Sterner, G. Waldstein, Storage of renewable energy in the natural gas grid, Erdoel Erdgas Kohle 126 (2010) 342.
[7] J. Baier, G. Schneider, A. Heel, A cost estimation for Co_2 reduction and reuse by methanation from cement industry sources in switzerland, Front. Energy Res. 6 (2018), https://doi.org/10.3389/fenrg.2018.00005.
[8] C. Jeong-Potter, R. Farrauto, Feasibility study of combining direct air capture of co_2 and methanation at isothermal conditions with dual function materials, Appl. Catal. B Environ. 282 (2021), https://doi.org/10.1016/j.apcatb.2020.119416.
[9] K. Akimoto, F. Sano, J. Oda, H. Kanaboshi, Y. Nakano, Climate change mitigation measures for global net-zero emissions and the roles of Co_2 capture and utilization and direct air capture, Energy Clim. Change 2 (2021), https://doi.org/10.1016/j.egycc.2021.100057.
[10] W. Li, H. Wang, X. Jiang, J. Zhu, Z. Liu, X. Guo, C. Song, A short review of recent advances in Co_2 hydrogenation to hydrocarbons over heterogeneous catalysts, RSC Adv. 8 (2018) 7651, https://doi.org/10.1039/c7ra13546g.
[11] S. Ewald, M. Kolbeck, T. Kratky, M. Wolf, O. Hinrichsen, on the deactivation of Ni-Al catalysts in co_2 methanation, Appl. Catal. A Gen. 570 (2019) 376, https://doi.org/10.1016/j.apcata.2018.10.033.
[12] T. Burger, F. Koschany, O. Thomys, K. Köhler, O. Hinrichsen, Co_2 methanation over Fe- and Mn-promoted Co-precipitated Ni-Al catalysts: synthesis, characterization and catalysis study, Appl. Catal. A Gen. 558 (2018) 44, https://doi.org/10.1016/j.apcata.2018.03.021.
[13] C.H. Bartholomew, Mechanisms of catalyst deactivation, Appl. Catal. A Gen. 212 (2001) 17, https://doi.org/10.1016/s0926-860x(00)00843-7.
[14] T. An Le, J. Kim, J.K. Kang, E.D. Park, Co and Co2 methanation over m (M = Mn, Ce, Zr, Mg, k, Zn, or V)-promoted ni/al@al_2o_3 catalysts, Catal. Today 348 (2020) 80, https://doi.org/10.1016/j.cattod.2019.08.058.
[15] W.L. Vrijburg, E. Moioli, W. Chen, M. Zhang, B.J.P. Terlingen, B. Zijlstra, I.A. W. Filot, A. Züttel, E.A. Pidko, E.J.M. Hensen, Efficient base-metal Ni-Mn/Tio_2 catalyst for Co_2 methanation, ACS Catal. 9 (2019) 7823, https://doi.org/10.1021/acscatal.9b01968.
[16] W.L. Vrijburg, G. Garbarino, W. Chen, A. Parastaev, A. Longo, E.A. Pidko, E.J. M. Hensen, Ni-Mn catalysts on silica-modified alumina for Co_2 methanation, J. Catal. 382 (2020) 358, https://doi.org/10.1016/j.jcat.2019.12.026.
[17] M.-A. Serrer, K.F. Kalz, E. Saraçi, H. Lichtenberg, J.-D. Grunwaldt, Role of iron on the structure and stability of $Ni_{3.2}Fe/Al_2o_3$ during dynamic co_2 methanation for p2x applications, ChemCatChem 11 (2019) 5018, https://doi.org/10.1002/cctc.201901425.
[18] K. Zhao, Z. Li, L. Bian, Co_2 methanation and co-methanation of co and co_2 over mn-promoted Ni/Al_2o_3 catalysts, Front. Chem. Sci. Eng. 10 (2016) 273, https://doi.org/10.1007/s11705-016-1563-5.
[19] A. Zhao, W. Ying, H. Zhang, M. Hongfang, D. Fang, Ni/Al_2o_3 catalysts for syngas methanation: effect of mn promoter, J. Nat. Gas. Chem. 21 (2012) 170, https://doi.org/10.1016/s1003-9953(11)60350-2.
[20] T. Franken, J. Terreni, A. Borgschulte, A. Heel, Solid solutions in reductive environment – a case study on improved co_2 hydrogenation to methane on cobalt based catalysts derived from ternary mixed metal oxides by modified reducibility, J. Catal. 382 (2020) 385, https://doi.org/10.1016/j.jcat.2019.12.045.
[21] D. Weber, K.M. Wadlinger, M.M. Heinlein, T. Franken, Modifying spinel precursors for highly active and stable Ni-based Co2 methanation catalysts, ChemCatChem 14 (2022), https://doi.org/10.1002/cctc.202200563.
[22] T. Burger, F. Koschany, A. Wenng, O. Thomys, K. Köhler, O. Hinrichsen, Simultaneous activity and stability increase of co-precipitated Ni–Al co_2 methanation catalysts by synergistic effects of fe and mn promoters, Catal. Sci. Technol. 8 (2018) 5920, https://doi.org/10.1039/c8cy01834k.
[23] A. Solis-Garcia, J.C. Fierro-Gonzalez, Mechanistic insights into the co_2 methanation catalyzed by supported metals: a review, J. Nanosci. Nanotechnol. 19 (2019) 3110, https://doi.org/10.1166/jnn.2019.16606.
[24] M. González-Castaño, J. González-Arias, L.F. Bobadilla, E. Ruíz-López, J. A. Odriozola, H. Arellano-García, In-situ drifts steady-state study of co_2 and co methanation over ni-promoted catalysts, Fuel 338 (2023), https://doi.org/10.1016/j.fuel.2022.127241.
[25] Q. Pan, J. Peng, T. Sun, S. Wang, S. Wang, Insight into the reaction route of co_2 methanation: promotion effect of medium basic sites, Catal. Commun. 45 (2014) 74, https://doi.org/10.1016/j.catcom.2013.10.034.
[26] Q. Pan, J. Peng, S. Wang, S. Wang, *In Situ* FTIR spectroscopic study of the Co_2 methanation mechanism on $Ni/Ce_{0.5}Zr_{0.5}O_2$, Catal. Sci. Technol. 4 (2014) 502, https://doi.org/10.1039/c3cy00868a.
[27] J. Ilsemann, M.M. Murshed, T.M. Gesing, J. Kopyscinski, M. Bäumer, On the support dependency of the Co_2 methanation – decoupling size and support effects, Catal. Sci. Technol. 11 (2021) 4098, https://doi.org/10.1039/d1cy00399b.
[28] X. Wu, L. Li, M. Song, H. Cai, J. Yang, G. Li, C. Hu, Insight into the impacts of mno_2 crystal phases on Co_2 selective hydrogenation to CH_4 on Ni/Mno_x catalysts, J. CO2 Util. 75 (2023), https://doi.org/10.1016/j.jcou.2023.102584.
[29] M.A.A. Aziz, A.A. Jalil, S. Triwahyono, R.R. Mukti, Y.H. Taufiq-Yap, M.R. Sazegar, Highly active Ni-promoted mesostructured silica nanoparticles for Co_2 methanation, Appl. Catal. B Environ. 147 (2014) 359, https://doi.org/10.1016/j.apcatb.2013.09.015.
[30] F.H. Chung, Quantitative interpretation of X-ray diffraction patterns of mixtures. I. Matrix-flushing method for quantitative multicomponent analysis, J. Appl. Crystallogr 7 (1974) 519, https://doi.org/10.1107/S0021889874010375.
[31] N. Rui, X. Zhang, F. Zhang, Z. Liu, X. Cao, Z. Xie, R. Zou, S.D. Senanayake, Y. Yang, J.A. Rodriguez, et al., Highly active Ni/Ceo_2 catalyst for Co_2 methanation: preparation and characterization, Appl. Catal. B Environ. 282 (2021) 119581, https://doi.org/10.1016/j.apcatb.2020.119581.
[32] D. Schmider, L. Maier, O. Deutschmann, Reaction kinetics of Co and co_2 methanation over nickel, Ind. Eng. Chem. Res. 60 (2021) 5792, https://doi.org/10.1021/acs.iecr.1c00389.
[33] A. Westermann, B. Azambre, M.C. Bacariza, I. Graça, M.F. Ribeiro, J.M. Lopes, C. Henriques, Insight into co_2 methanation mechanism over niusy zeolites: an operando IR study, Appl. Catal. B Environ. 174-175 (2015) 120, https://doi.org/10.1016/j.apcatb.2015.02.026.
[34] X. Jia, X. Zhang, N. Rui, X. Hu, C.-J. Liu, Structural effect of Ni/Zro_2 catalyst on Co_2 methanation with enhanced activity, Appl. Catal. B Environ. 244 (2019) 159, https://doi.org/10.1016/j.apcatb.2018.11.024.
[35] A. Cárdenas-Arenas, A. Quindimil, A. Davó-Quiñonero, E. Bailón-García, D. Lozano-Castelló, U. De-La-Torre, B. Pereda-Ayo, J.A. González-Marcos, J. R. González-Velasco, A. Bueno-López, *I*sotopic and in situ drifts study of the Co_2 methanation mechanism using Ni/CeO_2 and Ni/Al_2O_3 catalysts, Appl. Catal. B Environ. 265 (2020), https://doi.org/10.1016/j.apcatb.2019.118538.
[36] C. Li, Y.-W. Chen, Temperature-programmed-reduction studies of nickel oxide/alumina catalysts: effects of the preparation method, Thermochim. Acta 256 (1995) 457, https://doi.org/10.1016/0040-6031(94)02177-P.
[37] T. Engl, M. Langer, H. Freund, M. Rubin, R. Dittmeyer, Tap reactor for temporally and spatially resolved analysis of the Co_2 methanation reaction, Chem. Ing. Technol. 95 (2023) 658, https://doi.org/10.1002/cite.202200204.
[38] S. Fujita, M. Nakamura, T. Doi, N. Takezawa, Mechanisms of methanation of carbon dioxide and carbon monoxide over nickel/alumina catalysts, Appl. Catal. A Gen. 104 (1993) 87, https://doi.org/10.1016/0926-860x(93)80212-9.
[39] M. Agnelli, H.M. Swaan, C. Marquez-Alvarez, G.A. Martin, C. Mirodatos, CO hydrogenation on a nickel catalyst, J. Catal. 175 (1998) 117, https://doi.org/10.1006/jcat.1998.1978.
[40] J. Chen, X. Shen, Q. Wang, J. Wang, D. Yang, T. Bold, Y. Dai, Y. Tang, Y. Yang, Co_2 methanation over γ-Al_2O_3 nanosheets-stabilized ni catalysts: effects of MnO_x and

MoO_x additives on catalytic performance and reaction pathway, J. CO_2 Util. 63 (2022), https://doi.org/10.1016/j.jcou.2022.102113.
[41] Á. Szamosvölgyi, T. Rajkumar, A. Sápi, I. Szenti, M. Ábel, J.F. Gómez-Pérez, K. Baán, Z. Fogarassy, E. Dodony, B. Pécz, et al., Interfacial Ni active sites strike solid solutional counterpart in Co2 hydrogenation, Environ. Technol. Innov. 27 (2022) 102747, https://doi.org/10.1016/j.eti.2022.102747.
[42] G. Busca, V. Lorenzelli, Infrared spectroscopic identification of species arising from reactive adsorption of carbon oxides on metal oxide surfaces, Mater. Chem. 7 (1982) 89, https://doi.org/10.1016/0390-6035(82)90059-1.
[43] P.A.U. Aldana, F. Ocampo, K. Kobl, B. Louis, F. Thibault-Starzyk, M. Daturi, P. Bazin, S. Thomas, A.C. Roger, Catalytic Co_2 valorization into CH_4 on ni-based ceria-zirconia. reaction mechanism by operando ir spectroscopy, Catal. Today 215 (2013) 201, https://doi.org/10.1016/j.cattod.2013.02.019.
[44] A.H. Clark, J. Imbao, R. Frahm, M. Nachtegaal, ProQEXAFS: a highly optimized parallelized rapid processing software for QEXAFS data, J. Synchrotron Radiat. 27 (2020) 551, https://doi.org/10.1107/S1600577519017053.
[45] B. Ravel, M. Newville, Athena, Artemis, Hephaestus: data analysis for X-ray absorption spectroscopy using IFEFFIT, J. Synchrotron Radiat. 12 (2005) 537, https://doi.org/10.1107/S0909049505012719.